A Virtual Impedance-Based Control Bandwidth Enhancement Method for Three-Level Flying Capacitor Boost Converter

Kaidi Wang[1], Qiyu Li[1], Hongwei Zhou[2], Dapeng Lu[2], Cheng Luo[2]

[1] Shaanxi University of Science and Technology, Xi'an 710021, Shaanxi China；

[2] TBEA Xi'an Electric Technology Co., Ltd, Xi'an 710100, Shaanxi, China

Corresponding author: Kaidi Wang, 220612093@sust.edu.cn

Abstract

The control performance of photovoltaic generation system is highly dependent on the operating point position on the current-voltage curve. When the system operates in the near-constant dc-link voltage region, the control bandwidth of the system is small. This may bring about two problems: first, the MPPT period will be restricted, thus slow down the tracking process of the system; second, low bandwidth limits the speed of active power adjustment process.In this paper, the average state-space equation of the three-level flying capacitor boost converter used in PV inverters is first studied and derived, and then a strategy based on virtual impedance is proposed to improve the control bandwidth of the three-level flying capacitor boost converter. Finally, some simulation results show that the proposed virtual impedance strategy can achieve the expected effect of increasing the control bandwidth of the system.

Index Terms: three-level flying capacitor boost converter, control bandwidth, virtual impedance

1 Introduction

In the photovoltaic inverter system, the three-level flying capacitor boost converter is a feasible front-end voltage boost scheme [1, 2]. Compared with traditional two-level converters, three-level converters have the advantages of smaller current ripple and lower voltage stress [3, 4].

The output of PV array behaves as a nonlinear current-voltage(*I*–*V*) curve, leading to the variation of the control performance as the change of operating point position, in small-signal analysis, this nonlinear effect is represented by dynamic resistance, which is obtained from the slope of the *I*–*V* curve, and varies with PV voltage, irradiance, and cell temperature [5].In recent years, with the continuous improvement of economic efficiency and reliability requirements, the importance of PV nonlinear effects has increased [6].

In order to eliminating the influence of dynamic resistance and ensure the good control performance of the system, adaptive voltage control is first proposed in [7], [8]. According to this method, the dynamic resistance is estimated from the measured variables of the converter, and on this basis, the adaptive controller is designed. Although effective results are obtained, the implementation of this method is very complicated because the algorithm for estimating dynamic resistance is very complicated, and the parameters of the controller need to be updated constantly. Some papers have proposed control based on disturbance observer, which eliminates the bias of the system by estimating the uncertainty and disturbance, and also achieves certain results [9, 10]. However, due to the impossibility of accurate estimation, the control performance of the system cannot be guaranteed. A virtual impedance strategy is proposed to reduce the dynamic resistance transformation [3]. Series and parallel virtual resistors are used to improve the control performance, which also achieves certain results, but other virtual impedance types are not considered.

In this paper, a different approach based on virtual impedance emulation is adopted. This strategy avoids the influence of dynamic resistance on the control performance of the system, improves the control bandwidth of the system working near the open-circuit voltage, and verifies the effectiveness of the strategy through simulation. In the section 2 of this paper, the analyzed system is modeled, including the photovoltaic array model and the three-level flying capacitor boost converter model. In the section 3, the virtual impedance strategy used in this paper is proposed and compared with the traditional voltage-current dual circuit control strategy. On this basis, the effectiveness of the proposed strategy is verified with the simulation results in the section 4. Finally, the conclusion of this paper is drawn in section 5.

2 Converter System Model

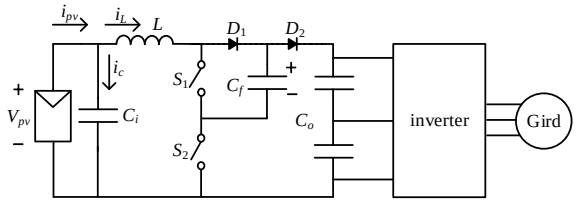

Fig. 1. Topology of three-level flying capacitor boost converter system used in photovoltaic inverters

The system analyzed in this paper is the three-level flying capacitor boost converter system used in photovoltaic inverters. Its topology is shown in Fig. 1, which includes input capacitor C_i, boost inductor L, flying-capacitor C_f, bus capacitor C_o, two switches S_1 and S_2, and two diodes D_1 and D_2. It is connected with the PV array of the front stage and the inverter system of the rear stage.

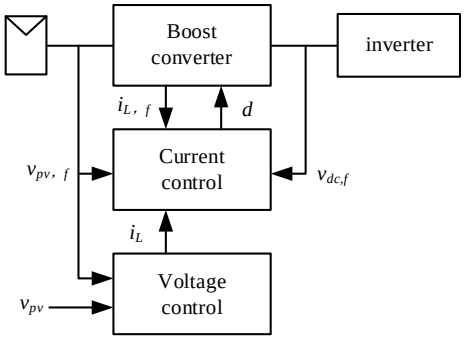

Fig. 2. Traditional photovoltaic voltage control structure

Traditional photovoltaic voltage regulation is carried out through cascaded feedback loops, in which the inner ring is the current ring, which controls the current of the inductor, and the outer ring is the voltage ring. The control structure is shown in Fig. 2, where d is the IGBT duty cycle, i_L is the reference current, and v_{pv} is the reference voltage. The measured variables were $i_{L,f}$ and $v_{pv,f}$.

2.1 Photovoltaic Array Model

PV array Is a five-parameter model, which uses luminescent current source (I_s), diode (I_0), series resistance (R_s) and shitter resistance (R_p) to represent the irradiance and temperature-related *I–V* characteristics of the module. The model of PV array is shown in Fig. 3.

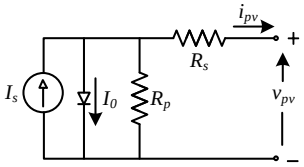

Fig. 3. Photovoltaic array model

According to Fig. 3, the *I–V* characteristic equation can be expressed as:

$$i_{pv} = I_s - I_0[\exp(\frac{v_{pv} + R_s i_{pv}}{V_t a}) - 1] - \frac{v_{pv} + R_s i_{pv}}{R_p} \quad (1)$$

Where I_s and I_0 are photovoltaic current and diode saturation current, and thermal voltage $V_t = N_s kT/q$ (k is Boltzmann constant; q is the electron charge; T is the temperature of the photovoltaic cell), R_s is the equivalent series resistance, and R_p is the equivalent parallel resistance.

Because PV arrays exhibit nonlinear behavior, small signal analysis is often employed in order to use linear modeling techniques. Through the characteristic *I–V* curve, $i_{pv} = f(v_{pv})$ changes with the PV voltage. The dynamic resistance (R_{pv}) of the PV module is defined as the ratio of small-signal PV voltage ($\hat{v}_{pv}$) to small-signal PV current ($\hat{i}_{pv}$), and the change of small-signal PV current can be obtained as [11]

$$R_{pv} = -\frac{\hat{v}_{pv}}{\hat{i}_{pv}} \Rightarrow \hat{i}_{pv} = -\frac{\hat{v}_{pv}}{R_{pv}} \quad (2)$$

The equation (2) shows that the $\hat{i}_{pv}$ change caused by the $\hat{v}_{pv}$ change depends on the dynamic resistance (R_{pv}). The resistance R_{pv} as a function of the operating point is highly variable and will become smaller at high voltages, high irradiance and high temperatures.

2.2 Three-level flying capacitor boost converter model

The modeling of the three-level flying capacitor converter should be run in continuous conduction mode, so there are four possible operating modes, as shown in the Fig. 4, when the duty cycle d<0.5, the converter will work in boost mode, then its operating modes are M00, M01 and M10, and the mode M11 is not used, its operation mode is… →M00→M01→M00→M10→…

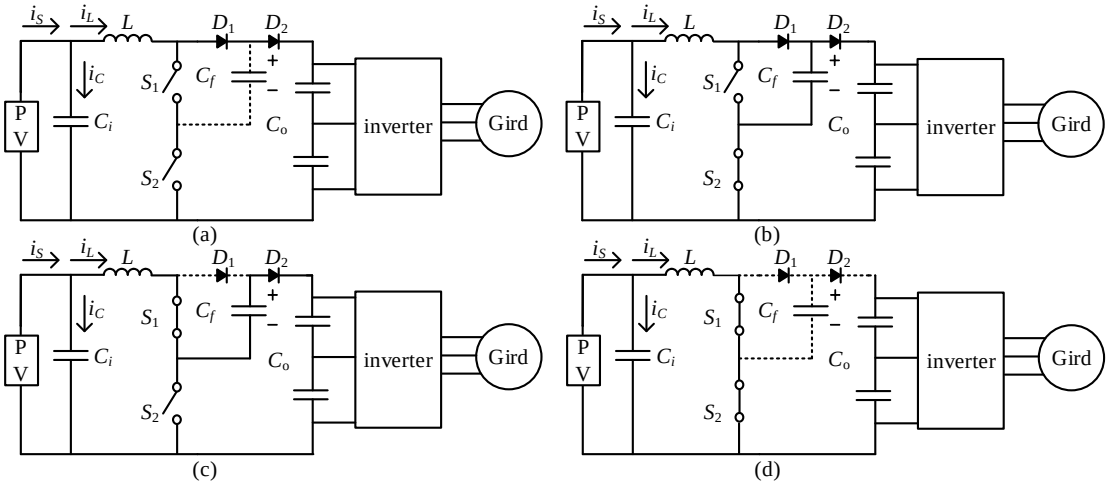

Fig. 4. Operating mode of a three-level flying capacitor boost converter(a)M00 (b)M01 (c)M10 (d)M11

Mode 1, M00

The two switches are disconnected in mode 1, as shown in Fig. 4(a). The state space equation is

$$\frac{d}{dt}\begin{bmatrix} i_L \\ v_C \\ v_{pv} \end{bmatrix} = \begin{bmatrix} 0 & 0 & \frac{1}{L} \\ 0 & 0 & 0 \\ -\frac{1}{C_i} & 0 & -\frac{1}{R_{pv}C_i} \end{bmatrix}\begin{bmatrix} i_L \\ v_C \\ v_{pv} \end{bmatrix} + \begin{bmatrix} -\frac{1}{L} \\ 0 \\ 0 \end{bmatrix} v_{dc} \quad (3)$$

Mode 2, M01

Switch S_1 is off and S_2 is closed, that is, switch mode 2, as shown in Fig. 4(b). The state space equation is

$$\frac{d}{dt}\begin{bmatrix} i_L \\ v_C \\ v_{pv} \end{bmatrix} = \begin{bmatrix} 0 & -\frac{1}{L} & \frac{1}{L} \\ \frac{1}{Cf} & 0 & 0 \\ -\frac{1}{C_i} & 0 & -\frac{1}{R_{pv}C_i} \end{bmatrix}\begin{bmatrix} i_L \\ v_C \\ v_{pv} \end{bmatrix} + \begin{bmatrix} 0 \\ 0 \\ 0 \end{bmatrix} v_{dc} \quad (4)$$

Mode 3, M10

Switch S_1 is closed and S_2 is off, that is, switch mode 3, as shown in Fig. 4(c). The state space equation is

$$\frac{d}{dt}\begin{bmatrix} i_L \\ v_C \\ v_{pv} \end{bmatrix} = \begin{bmatrix} 0 & \frac{1}{L} & \frac{1}{L} \\ -\frac{1}{C_f} & 0 & 0 \\ -\frac{1}{C_i} & 0 & -\frac{1}{R_{pv}C_i} \end{bmatrix}\begin{bmatrix} i_L \\ v_C \\ v_{pv} \end{bmatrix} + \begin{bmatrix} -\frac{1}{L} \\ 0 \\ 0 \end{bmatrix} v_{dc} \quad (5)$$

Table I Duty Cycle of Different Modes

Mode	Duty cycle
M00	1-2d_1
M01	d_1+ d_2
M10	d_1- d_2

The duty cycle of different modes in a switching period Ts is shown in Table I, where d_1 is the output duty cycle of voltage loop and current loop, and d_2 is the output duty cycle of flying capacitor voltage balancing loop. The influence of d_2 can be ignored during the design of virtual impedance. The converter is modeled using the method of average small signal modeling, and its average state space equation is

$$\frac{d}{dt}\begin{bmatrix} \langle i_L \rangle_{TS} \\ \langle v_C \rangle_{TS} \\ \langle v_{pv} \rangle_{TS} \end{bmatrix} = \begin{bmatrix} 0 & \frac{-2d_2}{L} & \frac{1}{L} \\ \frac{2d_2}{C_f} & 0 & 0 \\ -\frac{1}{C_i} & 0 & -\frac{1}{R_{pv}C_i} \end{bmatrix}\begin{bmatrix} \langle i_L \rangle_{TS} \\ \langle v_C \rangle_{TS} \\ \langle v_{pv} \rangle_{TS} \end{bmatrix} + \begin{bmatrix} \frac{d_1+d_2-1}{L} \\ 0 \\ 0 \end{bmatrix} V_{dc} \quad (6)$$

Considering the small signal perturbation, the two control signals can be expressed as

$$\begin{cases} d_1 = D_1 + \hat{d}_1 \\ d_2 = D_2 + \hat{d}_2 \end{cases} \quad (7)$$

In addition, small signal perturbations to state variables can be expressed as

$$\begin{cases} \langle i_L \rangle_{TS} = I_L + \hat{i}_L \\ \langle v_C \rangle_{TS} = V_C + \hat{v}_C \\ \langle v_{pv} \rangle_{TS} = V_{pv} + \hat{v}_{pv} \end{cases} \quad (8)$$

 DOI:10.30420/566414033

Therefore, the small signal equation of state for a three-level flying capacitor boost converter can be expressed in general form as follows

$$\begin{bmatrix} \hat{i}_L \\ \hat{v}_C \\ \hat{v}_{pv} \end{bmatrix} = \begin{bmatrix} \frac{V_{dc}(C_i R_{pv} s+1)}{LR_{pv}C_i s^2+Ls+R_{pv}} & \frac{-(C_i R_{pv} s+1)(2V_C-V_{dc})}{LR_{pv}C_i s^2+Ls+R_{pv}} \\ 0 & \frac{2I_L}{C_f s} \\ \frac{-R_{pv}V_{dc}}{LR_{pv}C_i s^2+Ls+R_{pv}} & \frac{R_{pv}(2V_C-V_{dc})}{LR_{pv}C_i s^2+Ls+R_{pv}} \end{bmatrix} \begin{bmatrix} d_1 \\ d_2 \end{bmatrix} \tag{9}$$

3 PV Voltage Control Strategy

3.1 Traditional Double Loop Control Strategy

The control block diagram of the traditional three-level flying capacitor converter is shown in the Fig. 5, where G_{icl} is the inner loop current loop, G_{cv} is the outer loop voltage loop controller, and G_{ci} is the current loop controller.

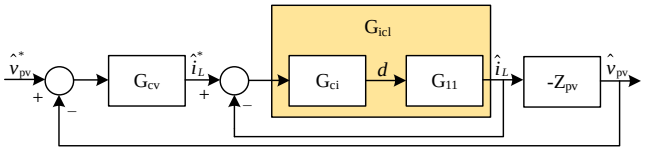

Fig. 5. The control block diagram of the traditional three-level flying capacitor converter

G_{11} is the duty cycle $\hat{d}$ to $\hat{i}_L$ transfer function, derived from the small signal model of the converter derived above

$$G_{11} = \frac{V_{dc}(C_i R_{pv} s+1)}{LR_{pv}C_i s^2+Ls+R_{pv}} \tag{10}$$

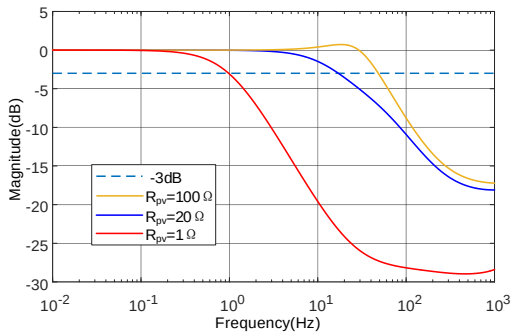

Fig. 6. The closed-loop bode diagram of PV voltage under different working conditions

According to the control block diagram, the closed-loop bode diagram of PV voltage under three different working conditions is obtained: near open circuit voltage (R_{pv}=1Ω); Voltage near MPP point (R_{pv}=20Ω); And lower than MPP point voltage (R_{pv}=100Ω), as shown in the Fig. 6. It can be observed that the dynamic resistance has a great influence on the control bandwidth of the system, especially when operating at near open circuit voltage, the bandwidth is reduced.

3.2 Virtual Impedance Control Strategy

A direct strategy to reduce the effect of dynamic resistance changes in a PV array is to add an impedance Z_{real} in parallel with the PV array, such as a small resistance or a large capacitance. If this impedance is small enough around the frequency of interest, then the system will behave as this known impedance, thus eliminating the effect of changes in the controlled object.

$$Z_{eq,real} = -\frac{\hat{v}_{pv}}{\hat{i}_{pv}} = R_{pv} // Z_{real} \tag{11}$$

Because the required impedance is too small for practical applications and can result in higher costs or additional power losses to the system, it is simulated in the control strategy. The actual PV voltage control loop is shown in Fig. 7 (a), where Z_{real} is the real resistance, $\hat{i}_Z$ and $\hat{i}_{RC}$ pass through this impedance and the current of the PV array and input capacitor combination, respectively. Similarly, the voltage loop of the virtual impedance is shown in Fig. 7(b), where Z_p is the virtual parallel impedance, $\hat{i}_{ZP}$ is the current flowing through the impedance, and $\hat{i}_V$ is the virtual current.

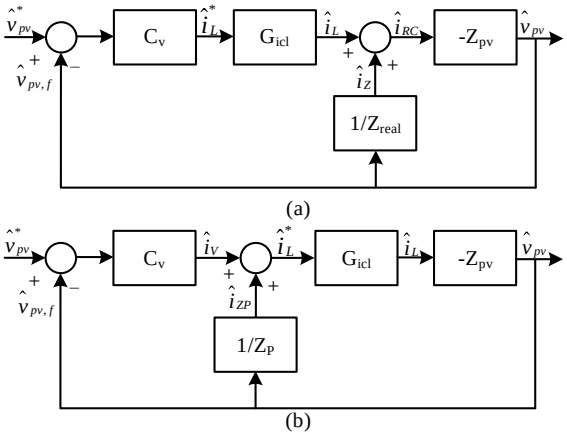

Fig. 7. PV voltage control loop (a) Actual parallel impedance Z_{real} (b) Virtual parallel impedance Z_p

In the various virtual impedances envisaged by the three-level flying capacitor boost converter, namely R, RC, RL and RLC, the high frequency impedances are higher when the inductor is present, and the voltage harmonics that occur in the PV voltage measurement are not amplified; When capacitors are present, the DC impedance is infinite, while in other cases it is lower. Therefore, in these four possibilities, the virtual impedance is chosen as the series form of the RLC.

In order to further reduce the impedance variation in the controller, the virtual impedance in series with the PV array is added on the basis of the parallel virtual impedance above, and the equivalent circuit is obtained as shown in the Fig. 8 (a), where R_s is the virtual series impedance, v_{Rs} is the voltage drop on the impedance, and v_v is the virtual voltage. The control loop of the new photovoltaic voltage is shown in the Fig. 8 (b).

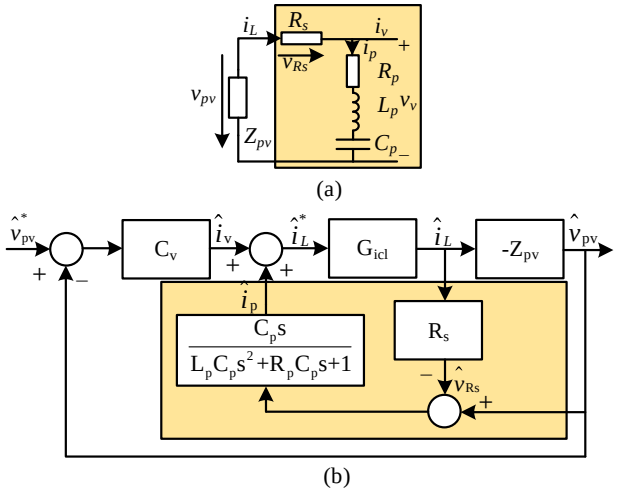

Fig. 8. (a) New equivalent circuit (b)New PV voltage control loop

In this case, the equivalent impedance Z_{eq} in the controller is

$$Z_{pv} = -\frac{\hat{v}_{pv}}{\hat{i}_L} = \frac{R_{pv}}{C_{in}R_{pv}s+1} \tag{12}$$

$$Z_{eq} = \frac{Z_{pv}Z_p}{Z_{pv}+Z_s+Z_p} = \frac{Z_{pv}(R_p+sL_p+1/C_ps)}{Z_{pv}+R_s+R_p+sL_p+1/C_ps} \tag{13}$$

It can be seen from equation (12) that Z_{pv} changes with the change of R_{pv}. When virtual impedance is added, Z_{pv} is equivalent to Z_{eq}, and its expression is shown in Equation (13). According to equation (13), when R_s+R_p=0, Z_{eq} expression is shown as equation (14). It can be seen from this expression that sL_p and $1/sC_p$ can be ignored at a certain frequency by selecting the values of L_p and C_p. When sL_p and $1/sC_p$ are ignored, Z_{eq} is approximately equal to R_p, thus eliminating the influence of R_{pv} on the controlled object. Therefore, the design value of R_s is - R_p, which weakens the influence of R_{pv} in the bandwidth range of the voltage loop.

$$Z_{eq} = \frac{Z_{pv}(R_p+sL_p+1/C_ps)}{Z_{pv}+sL_p+1/C_ps} \tag{14}$$

The design principle of R_p is to maximize the bandwidth of the control loop while maintaining the stability of the control loop. First of all, according to the bode diagram of the voltage loop and the current loop transfer function, the PI parameters v_{pv_kp} and v_{pv_ki} of the voltage loop are determined first, and the PI parameters i_{L_kp} and i_{L_ki} of the current loop are determined. This process is relatively mature, which is omitted here. Then, according to the control loop after adding the virtual impedance, the closed-loop transfer function G_{vpv_cl} of the voltage loop is obtained, as shown in equation (15).

$$G_{Vpv\_cl} = \frac{As^2+Bs+C}{Ds^4+Es^3+Fs^2+Gs+H} \tag{15}$$

$$A = -R_{pv}V_{dc}Z_pi_{L\_kp}v_{pv\_kp} \quad ;$$

$$B = -R_{pv}V_{dc}Z_pi_{L\_ki}v_{pv\_kp} - R_{pv}V_{dc}Z_pi_{L\_kp}v_{pv\_ki} \quad ;$$

$$C = -R_{pv}V_{dc}Z_pi_{L\_ki}v_{pv\_ki} \quad ; \quad D = C_iLR_{pv}Z_pe^{(T_ds)}s^4 \quad ;$$

$$E = LZ_pe^{(T_ds)} + C_iR_{pv}V_{dc}Z_pi_{L\_kp} + C_iR_{pv}V_{dc}Z_si_{L\_kp} \quad ;$$

$$F = R_{pv}V_{dc}i_{L\_kp} + V_{dc}Z_pi_{L\_kp} + V_{dc}Z_si_{L\_kp} + R_{pv}Z_pe^{(T_ds)} + C_iR_{pv}V_{dc}i_{L\_ki}(Z_p+Z_s) - R_{pv}V_{dc}Z_pi_{L\_ki}v_{pv\_kp} \quad ;$$

$$G = R_{pv}V_{dc}i_{L\_ki} + V_{dc}Z_pi_{L\_ki} + V_{dc}Z_si_{L\_ki} - R_{pv}V_{dc}Z_p(i_{L\_ki}v_{pv\_kp} + i_{L\_kp}v_{pv\_ki}) \quad ;$$

$$H = -R_{pv}V_{dc}Z_pi_{L\_ki}v_{pv\_ki} \ .$$

Where T_d is the delay time of the digital control system, Z_p= (R+$L_p$$s$+1/$C_p$$s$), Z_s=R_s.

According to the transfer function, select different virtual impedance parameters to draw the closed-loop functional bode diagram as shown in Fig. 9. First, determine the value of virtual resistance. According to the bode diagram of G_{vpv_cl}, it can be seen that the larger the R_p, the larger the bandwidth of the control ring, so the value of R_p can be selected according to the bode diagram of G_{vpv_cl} for experimental debugging. In addition, R_p has a lower limit, too small R_p will cause the bandwidth of the voltage loop cannot be improved, and will cause the $\hat{i}_P$ to be too large, making the loop of the virtual impedance unstable.

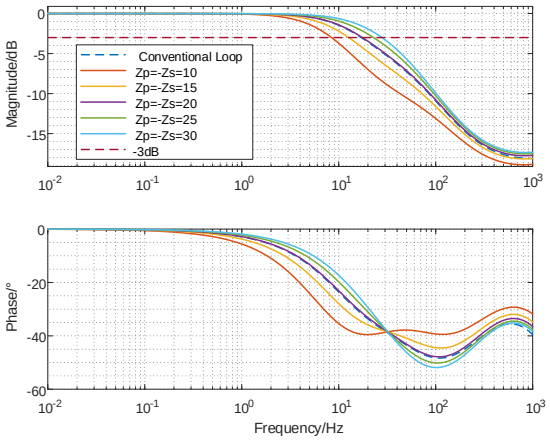

Fig. 9. PV voltage closed-loop bode diagram with different Zp values

After the R_p value is selected, the values of L_p and C_p are taken the same way. On the basis of the R_p value

 DOI:10.30420/566414033

determination, different L_p values are first taken to observe the change trend of the system control bandwidth, and then different C_p is added to observe the change trend of the system bandwidth on this basis, and finally a set of parameters is determined as the basis of simulation and experiment debugging.

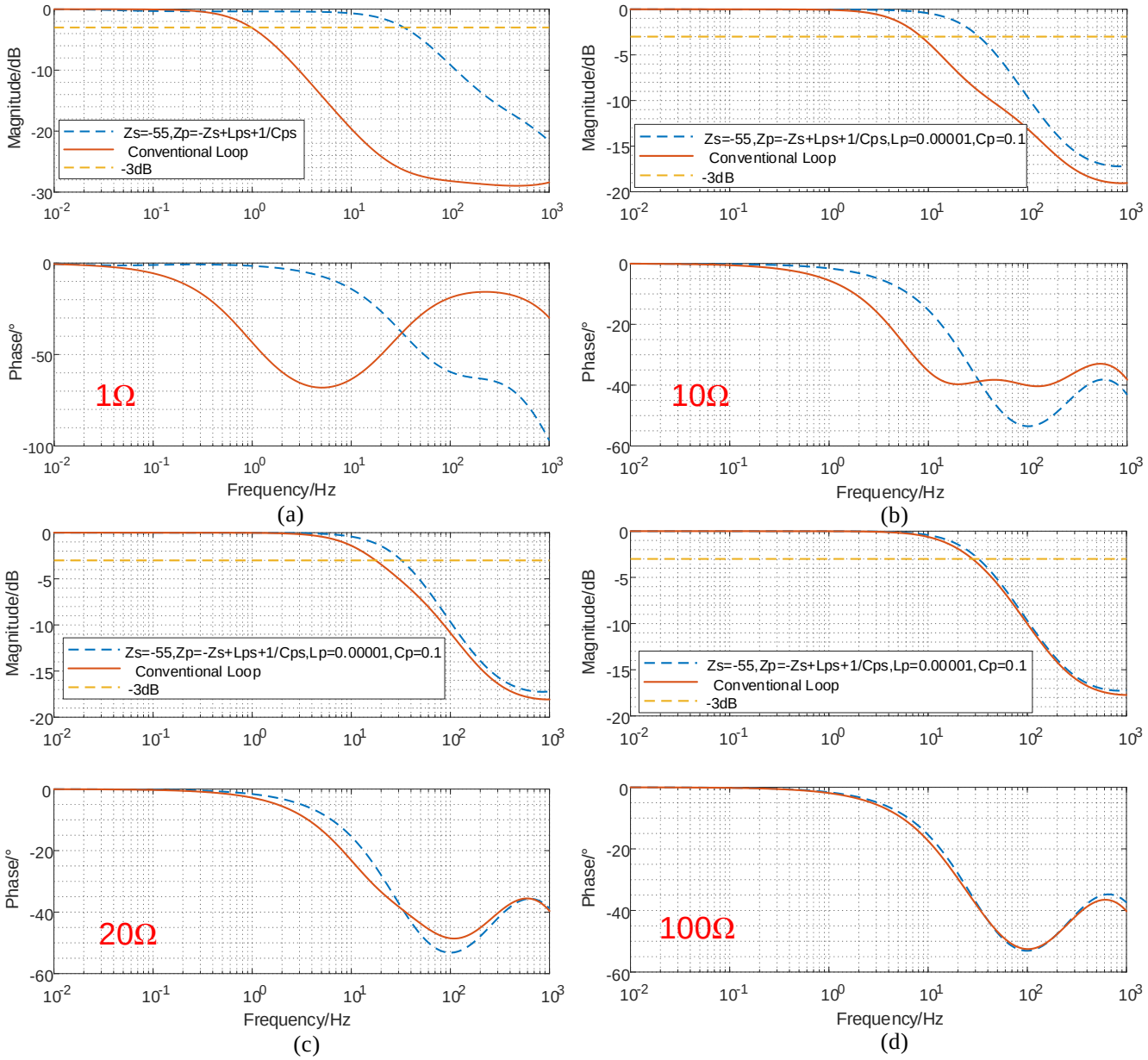

Fig. 10. The closed-loop bode diagrams at different operating points under two control strategies (a) R_{pv}=1Ω, (b) R_{pv}=10Ω, (c) R_{pv}=20Ω, (d) R_{pv}=100Ω

The closed-loop bode diagrams at different operating points under two control strategies are drawn as shown in the Fig. 10: near open circuit voltage (R_{pv}=1Ω, as shown in Fig. 10 (a)); Lower than the open circuit voltage (R_{pv} =10Ω, as shown in Fig. 10 (b)) near the MPP point voltage (R_{pv} =20Ω, as shown in Fig. 10 (c)); And lower than MPP point voltage (R_{pv} =100Ω, Fig. 10 (d)). It can be observed that in different working states, the control strategy using virtual impedance strategy has a larger system control bandwidth, and the system control performance has been greatly improved.

4 Simulation Result

The features of the three-level flying capacitor boost converter and the PV array used throughout the paper are given in Tables II and III, respectively.

 DOI:10.30420/566414033

Table II Parameter of The Three-Level Flying Capacitor Boost Converter

Parameter	Value
Input capacitor C_i	3.5e-6 F
Boost inductor L	276.71e-6 H
Flying capacitor C_f	20e-6 F
Output capacitor C_o	1e-5 F
Switching frequency f_s	16 kHz
Bus voltage	1300 V

Table III Features of The PV Array

Parameter	Value
Peak power	38367 W
Mpp voltage V_{mpp}	870 V
Mpp current I_{mpp}	44.1 A
Open-circuit voltage V_{oc}	1089 V
short-circuit current I_{sc}	47.04 A

Fig. 11 shows two PV voltage waveforms under the traditional strategy and the virtual impedance strategy proposed in this paper, when the PV reference voltage suddenly decreases from 1000V to 900V. It is clearly shown that the virtual impedance strategy proposed in this paper for the three-level flying capacitor boost converter can significantly improve the control bandwidth of PV voltage.

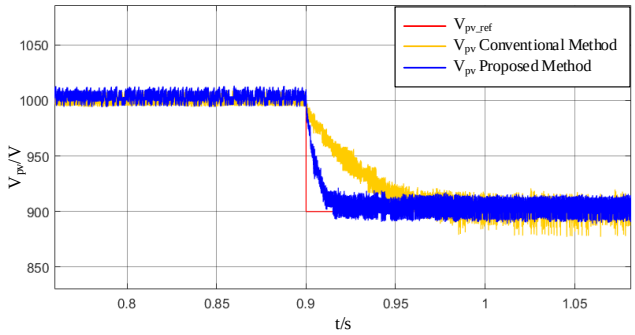

Fig. 11. V_{pv_ref} changes from 1000V to 900V, PV voltage under two different strategies

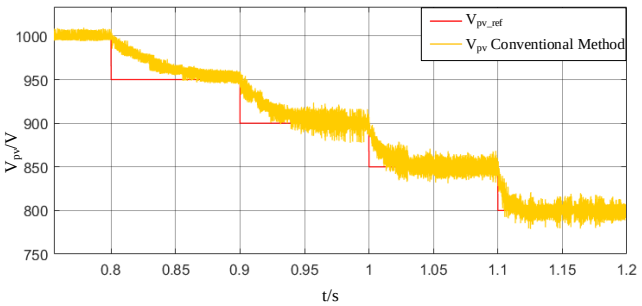

Fig. 12. Simulation of the PV voltage regulation for the traditional control.

Fig. 12 shows the PV voltage waveform under the traditional control strategy, when the PV reference voltage starts from 1000V and decreases from 50V to 800V. As deduced above, the control performance of the converter system varies greatly with the change of the operating points on the photovoltaic curve, and the control response is very slow near the open circuit voltage.

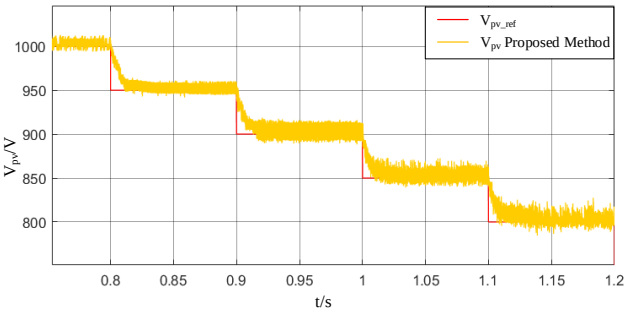

Fig. 13. Simulation of the PV voltage regulation for the virtual impedance control.

Fig. 13 shows the PV voltage waveform under the virtual impedance control strategy proposed in this paper, when the PV reference voltage starts from 1000V and decreases from 50V to 800V. As can be observed in Fig. 13, the voltage response is very fast for the whole operating range, including very small R_{pv} values. When comparing these results with the traditional control (As shown in Fig 12), it is clear that the control performance has been greatly improved.

The simulation results are consistent with the theoretical analysis above, which proves that the virtual impedance strategy proposed in this paper effectively reduces the influence of dynamic resistance on the control performance of the system, and effectively improves the control performance of the three-level flying capacitor boost converter system, which plays a positive role in the entire photovoltaic inverter system.

5 Conclusion

This paper first modeled the studied system, including photovoltaic array and three-level flying capacitor boost converter. On this basis, a photovoltaic voltage control strategy based on virtual impedance was proposed. Compared with the traditional voltage-current double-loop control strategy, the influence of photovoltaic array dynamic resistance on system control performance was avoided, and the control bandwidth of the system was improved. The speed of power scheduling of photovoltaic inverter is accelerated. The bode diagram of PV voltage closed loop and the simulation results show that the virtual impedance strategy proposed in this paper is effective.

ISBN 978-3-8007-6414-3

6 References

[1] Y. Zhang, J. Shi, L. Zhou, J. Li, M. Sumner, P. Wang and C. Xia, “Wide input-voltage range boost three-level DC-DC converter with quasi-Z source for fuel cell vehicles,” *IEEE Trans. Power Electron.*, vol. 32, no. 9, pp. 6728–6738, Sep. 2017.

[2] H. Watanabe, K. Kusaka, K. Furukawa, K. Orikawa and J. I. Itoh, “DC to single-phase AC voltage source inverter with power decoupling circuit based on flying capacitor topology for PV system,” in *Proc. IEEE 31st Appl. Power Electron. Conf.*, pp. 1336–1343, 2016.

[3] L. G. Franquelo et al., “The age of multilevel converters arrives,” IEEE Ind. Electron. Mag., vol. 2, no. 2, pp. 28–39, Jun. 2008.

[4] S. Kouro, M. Malinowski, K. Gopakumar, J. Pou, L. G. Franquelo, B. Wu, J. Rodriguez, M. A. Perez, and J. I. Leon, “Recent advances and industrial applications of multilevel converters,” IEEE Trans. Ind. Electron., vol. 57, no. 8, pp. 2553–2580, Aug. 2010.

[5] Andoni Urtasun, Ernesto L. Barrios, and Luis Marroyo, “Control of a Photovoltaic Array Interfacing Current-Mode-Controlled Boost Converter Based on Virtual Impedance Emulation,” IEEE Trans. Ind. Electron., VOL. 66, NO. 5, MAY 2019.

[6] S. M. Tayebi and I. Batarseh, “Mitigation of current distortion in a threephase microinverter with phase skipping using a synchronous sampling dc-link voltage control,” IEEE Trans. Ind. Electron., vol. 65, no. 5, pp. 3910– 3920, May 2018.

[7] A. Urtasun, P. Sanchis, and L. Marroyo, “Adaptive voltage control of the dc/dc boost stage in PV converters with small input capacitors,” IEEE Trans. Power Electron., vol. 28, no. 11, pp. 5038–5048, Nov. 2013.

[8] M. Sitbon, S. Schacham, T. Suntio, and A. Kuperman, “Improved adaptive input voltage control of a solar array interfacing current mode controlled boost power stage,” *Energy Convers. Manag.*, vol. 98, pp. 369–375, 2015.

[9] M. Sitbon, S. Schacham, and A. Kuperman, “Disturbance observerbased voltage regulation of current-mode-boost-converter-interfaced photovoltaic generator,” *IEEE Trans. Ind. Electron.*, vol. 62, no. 9, pp. 5776– 5785, Sep. 2015.

[10] R. Errouissi, A. Al-Durra, and S. M. Muyeen, “A robust continuous time MPC of a DC-DC boost converter interfaced with a grid-connected photovoltaic system,” *IEEE J. Photovolt.*, vol. 6, no. 6, pp. 1619–1629, Nov. 2016.

[11] M. G. Villalva, T. G. de Siqueira, and E. Ruppert, “Voltage regulation of photovoltaic arrays: Small-signal analysis and control design,” IET Power Electron., vol. 3, no. 6, pp. 869–880, 2010.